HHS Public Access

Author manuscript

Biochem J. Author manuscript; available in PMC 2026 April 08.

Published in final edited form as:

Biochem J. 2026 April 08; 483(4): 409–427. doi:10.1042/BCJ20250278.

Serendipitous Discovery of an Allosteric Inhibitor Binding Groove in the Proline Biosynthetic Enzyme Pyrroline-5-Carboxylate Reductase 1 (PYCR1)

Kaylen R. Meeks[1], **Caitlin J. Mattingly**[1], **Jay C. Nix**[2], **Oleksii Chuk**[3,4], **Mykola V. Protopopov**[3,5], **Olga O. Tarkhanova**[3], **John J. Tanner**[1,6,*]

[1]Department of Biochemistry, University of Missouri, Columbia, Missouri 65211, United States

[2]Molecular Biology Consortium, Advanced Light Source, Lawrence Berkeley National Laboratory, Berkeley, CA 94720, USA.

[3]Chemspace LLC, Akademika Kukharya Str, 7, building 146, unit M, Kyiv, 02094, Ukraine

[4]Palladin Institute of Biochemistry, National Academy of Sciences of Ukraine, Leontovycha Street 9, Kyiv, 01054, Ukraine

[5]Taras Shevchenko National University of Kyiv, Kyiv 01033, Ukraine.

[6]Department of Chemistry, University of Missouri, Columbia, Missouri 65211, United States

Abstract

Δ^1-pyrroline-5-carboxylate (P5C) reductase 1 (PYCR1) catalyzes the NAD(P)H-dependent conversion of L-P5C to L-proline and is one of the most consistently upregulated metabolic enzymes in cancer cells. High PYCR1 expression is associated with adverse clinical outcomes, and its knockdown inhibits tumor proliferation and metastasis, motivating inhibitor discovery. All structurally validated PYCR1 inhibitors to date bind in the active site and are anchored in the L-P5C binding pocket by an anionic functional group, typically carboxylate. Seeking inhibitors with alternative anchors, we used X-ray crystallography to screen 22 fragment-like compounds (MW = 189–343 Da) from docking that represent six different carboxylic acid isosteres. Surprisingly, only one compound bound in the active site. Four other compounds were found in three adjacent remote sites located in oligomer interfaces. The compounds bind 7 Å from NADH and 10–14 Å from L-P5C, and the intervening space is blocked by protein for inhibitors in Sites 1A/1B and open for inhibitors in Site 2. Together, the three binding sites define a ligand binding hot spot groove that spans 33 Å. The remote binders inhibit PYCR1 activity with K values from the

[*]**Corresponding author:** Department of Biochemistry, University of Missouri, Columbia, MO 65211. tannerjj@missouri.edu.

CRediT Author Contributions

K.R.M.: Conceptualization, Methodology, Investigation, Writing-Original Draft, Writing-Review & Editing, Visualization, Validation. C.J.M.: Investigation and Visualization. J.C.N.: Investigation. O.C.: Investigation. M.V.P.: Conceptualization, Investigation. O.T.: Conceptualization, Investigation. J.J.T.: Conceptualization, Writing-Original Draft, Writing-Review & Editing, Visualization, Validation, Supervision, Project administration, Funding acquisition.

Statement of Competing Interests

The work described herein was produced by a joint collaboration between employees of the University of Missouri and Chemspace LLC. Chemspace is a company that offers hit discovery services in ultra-large chemical spaces followed by sourcing and procurement of the identified hits.

mixed model of inhibition of 32 μM to 2 mM. Co-crystal structures of PYCR1 with combinations of allosteric inhibitors, NADH, and L-P5C/proline analogs suggest the inhibitors can bind to the ternary PYCR1-L-P5C-NAD(P)H complex in addition to the free enzyme, consistent with a mixed mechanism of inhibition. The discovery of an allosteric inhibitor binding groove that accommodates multiple fragments heralds a new era of PYCR1 inhibitor design.

Keywords

X-ray crystallography; allosteric inhibitors; enzyme inhibition; proline biosynthesis; carboxylic acid bioisosteres; fragment-based drug discovery

Introduction

Proline metabolism, comprising proline biosynthetic and catabolic pathways, has important roles in cancer cell growth and metastasis (1–3). The final step in proline biosynthesis is catalyzed by Δ^1-pyrroline-5-carboxylate (P5C) reductase (PYCR). PYCRs generate L-proline by catalyzing the reduction of L-P5C in a NAD(P)H-dependent reaction (Figure 1). Of the three major PYCR enzymes in humans, PYCR1 is most associated with cancer progression (4). PYCR1 forms a mitochondrial metabolic hub, known as the proline cycle, with the proline catabolic enzyme proline dehydrogenase, which catalyzes the FAD-dependent oxidation of L-proline to L-P5C. The proline cycle supports ATP production, protein and nucleotide synthesis, anaplerosis, and redox homeostasis in cancer cells, and the enzymes of the proline cycle have emerged as targets of inhibition (2, 3, 5).

PYCR1 plays important roles in the metabolism of cancer cells. The *PYCR1* gene is upregulated in many cancers (4). The high expression of *PYCR1* correlates with tumor aggressiveness and poor patient outcomes, and the knockdown of the *PYCR1* gene results in decreased tumor proliferation and metastasis (4, 6–14). In addition to the correlative data, the cellular mechanisms of PYCR1 in cancer are being revealed. For example, cells with high *PYCR1* expression are less sensitive to TNF-related apoptosis-inducing ligand (TRAIL), a cytokine that causes apoptosis in tumor cells (15). Proline metabolism regulates the crosstalk between cancer cells and the tumor microenvironment, influencing tumor progression by contributing to the synthesis of proline-rich collagen, shaping the immune tumor microenvironment and hence the efficacy of immune therapy in cancer patients (16). PYCR1 was shown to interact with EGFR, promoting esophageal squamous cell carcinoma progression and metastasis by activating the PI3K/AKT/mTOR signaling pathways, which are integral to the aggressive behavior of the disease (17). In bladder cancer, hypoxia-induced PYCR1 enhances glycolysis, leading to increased lactate production and elevated H3K18la levels, which upregulates SLC6A14 transcription and glutamine catabolism, thereby promoting tumor growth and metastasis (18). The accumulating data showing the involvement of PYCR1 in cancer cell growth, metabolism, and metastasis has motivated inhibitor development.

PYCR1 inhibitor discovery research has explored proline analogs (MW < 150 Da) (19, 20), diverse fragments (115–300 Da) (21), and a focused library of fragment-like carboxylic acids identified from template docking (143–289 Da) (22). These studies have generated

several structurally-validated compounds that target the active site and inhibit PYCR1 with micromolar affinity. The crystal structures of PYCR1-inhibitor complexes revealed a conserved binding mode in which an anionic group (carboxylate or sulfonate) anchors the inhibitor in the αK-αL loop of the L-P5C substrate binding pocket. The anchoring group forms several hydrogen bonds with the backbone and side chains of the substrate loop, as well as a conserved water molecule. A conclusion from this work is that molecular anchors that mimic the carboxylate of the substrate L-P5C are important for targeting inhibitors to the active site.

The intended goal of this study was to diversify and improve the pharmacological properties of PYCR1 inhibitors by exchanging the carboxylate anchor with bioisosteres. Whereas the carboxylic acid group is found on many drug molecules (over 450 marketed drugs in 2010 contained the group), it can be associated with poor cell membrane permeability and toxicity (23–26). The goals of bioisosteric replacement are to enhance pharmacological properties such as permeability, metabolic stability and pharmacokinetics while minimizing toxicity and maintaining good binding to the target (27). Common carboxylic acid bioisosteric groups include sulfonic/sulfinic acid, hydroxamic acid/ester, phosphonic/phosphinic acid, sulfonamide, nitro group, 5-oxo-1,2,4-oxadiazole, and tetrazole.

Here, we tested 22 compounds selected from virtual ligand screening that contain carboxylic acid isosteres, including sulfonic acid, hydroxamic acid, sulfonamide, nitro group, 5-oxo-1,2,4-oxadiazole, and tetrazole (Figure 2). Docking predicted that these compounds should target the active site with the isostere bound in the substrate binding loop. The library was screened using X-ray crystallography, and compound **8** was identified as binding in the active site, as predicted. However, a more detailed analysis of the electron density maps revealed that four other compounds (**4**, **5**, **9**, and **10**) were bound in remote sites located within the oligomer interfaces of the PYCR1 decamer. The remote sites form a ligand binding hotspot groove that spans 33 Å. All four remote binders inhibit PYCR1 enzymatic activity. The allosteric inhibitors make few electrostatic interactions with the enzyme, suggesting that binding is driven by shape complementary and nonpolar interactions. Our results suggest new approaches for developing novel PYCR1 inhibitors.

Results

The compound library

Commercially available compounds were identified from virtual screening of a 1519-compound library comprising sulfonic acids and bioisosteres of carboxylic acids. Docking was consistent with the compounds binding in the active site with the carboxylic acid isostere group anchored in the αK-αL loop of the L-P5C substrate binding pocket. Based on docking scores and visual inspection of binding modes, 22 compounds were selected for experimental testing against PYCR1. The final set of 22 compounds spans a molecular weights range of 189 to 343 Da and includes six classes of carboxylic acid bioisosteres: sulfonic acid, hydroxamic acid, sulfonamide, nitro group, 5-oxo-1,2,4-oxadiazole, and tetrazole (Figure 2). We note that compounds **8**, **12**, and **13** are close analogs of known PYCR1 inhibitors from Meeks et al. (22) (Tanimoto coefficients based on based on MACCS fingerprints of 0.54–0.65).

Primary experimental screening by X-ray crystallography

X-ray crystallography was used as the primary experimental screen with electron density as the readout to prioritize the discovery of binders. Each compound in the library was co-crystallized with PYCR1. Eighteen were co-crystallized at 25 mM compound concentration, while **1**, **12**, **13**, and **20** were co-crystallized at lower concentrations due to lower solubility in aqueous buffer or difficulties in obtaining good crystals. Additional compound (11–50 mM) was added to the cryo-buffer (20% (v/v) PEG 200) during crystal harvesting.

Convincing electron density was observed for five compounds in the primary screen (**4**, **5**, **8, 9**, **10**). Surprisingly, only one compound bound in the active site as predicted (**8**). The other four hit compounds (**4**, **5**, **9**, **10**) were found in remote sites located in oligomer interfaces. Because of the potential for discovering the first allosteric inhibitors of PYCR1, we focused on validating the remote binders.

Follow-up validation X-ray crystallography was performed with the remote binders using higher compound concentrations and/or better crystals to definitively resolve the poses and interactions with the enzyme. In total, eight crystal structures in the resolution range of 1.5 – 1.8 Å were determined, including binary PYCR1-inhibitor complexes for **4**, **5**, **9**, and **10** (Table 1), quaternary PYCR1-inhibitor-NADH-proline analog complexes for **4**, **9** and **10** (Table 2), and a unique ternary PYCR1-**5**-proline analog complex in which **5** is bound at two distinct remote sites and the NADH site (Table 2).

Summary of PYCR1 structure and overview of the allosteric groove

The fold, oligomeric structure, and coenzyme/substrate binding sites of PYCR1 have been charactered by high resolution X-ray crystallography (28). PYCR1 has a two-domain fold consisting of an N-terminal Rossmann fold dinucleotide-binding domain and a C-terminal α-helical domain, which functions both in oligomerization and binding the substrate L-P5C (Figure 3A). NADPH binds at the C-termini of the strands of the Rossmann fold domain, while L-P5C is anchored in the loop connecting helices K and L of the C-terminal domain (αK-αL loop). Two protomers assemble into a domain-swapped dimer that brings the αK-αL loop of one protomer close to the coenzyme of the other protomer, hence dimerization is essential for building the functional active site (Figure 3B). Five of the domain-swapped dimers assemble into a pentamer-of-dimers decamer having D_5 symmetry, which is described by one 5-fold axis and five 2-fold axes (Figure 3C and Supplementary Figure S1A). The 2-fold axes are perpendicular to the 5-fold axis and intersect at the center of the decamer. The decamer has 10 complete active sites. Sedimentation velocity studies have shown that the decamer is formed in solution (28). The asymmetric unit of the *C*2 crystal form used here contains five chains, labeled A-E, which form 2.5 dimers. Chains A and B form a dimer, as do chains C and D (Figure 3D and Supplementary Figure S1A). Two-fold crystallographic symmetry generates the other 2.5 dimers of the decamer.

The allosteric inhibitors bind in oligomer interfaces near the 2-fold symmetry axes of the decamer. An overview of the remote binding sites is shown in the composite model of the decamer viewed down a 2-fold axis (Figure 3D and Supplementary Figure S1A). In this orientation, two copies of **4** are seen near the 2-fold axis in locations labeled Site 1A and

Site 1B. Compound **5** also binds in Site 1A but apparently not in Site 1B (**5** omitted in Figure 3 for clarity). Compounds **9** and **10** bind farther from the 2-fold axis in Site 2, as shown for **9** in Figure 3D (**10** omitted in Figure 3 for clarity). Together, the three remote binding sites form a ~33 Å groove that intersects the NAD(P)H pocket (Figure 3D, 3E). The D_5 symmetry implies there are five pairs of allosteric grooves (10 total) per decamer.

The poses of the allosteric inhibitors are not influenced by crystal contacts. The allosteric inhibitors bind near two-fold axes of the decamer and this region of the protein surface is not involved in crystal packing interactions. The bound inhibitors contact solvent-filled cavities in the crystal lattice (Supplementary Figure S1B, S1C). The closest contact of an inhibitor to another decamer in the lattice is 8 Å and occurs only for the instances of compounds **4** and **5** bound to chain E. This distance is safely beyond the interaction distances of hydrogen bonding (< 3.2 Å) and van der Waals contacts (< 4.0 Å). The next closest crystal contact of the other instances of **4** and **5** is 14 Å. For compounds **9** and **10**, the closest contact to another decamer is greater than 18 Å. Thus, the poses and interactions observed in the crystal structures accurately reflect those occurring in solution.

Poses and interactions of compounds 4 and 5 in allosteric Sites 1A and 1B

The structure of PYCR1 complexed with **4** was determined at 1.74 Å resolution. Compound **4** has two poses corresponding to aforementioned Sites 1A and 1B. **4** in pose 1A has strong electron density in all five chains of the asymmetric unit with occupancies ranging from 0.89 to 0.95 (Figure 4A). This site is in the dimer interface, and the compound interacts with two protomers. The interaction surface is composed of helices αJ and αK of one protomer and αA and 3/10 helix F from a different protomer (secondary structure labeling from Christensen et al. (28)). Ligand interactions calculated with LigPlot+ (29) are shown in Supplementary Figure S2. Nonpolar interactions are prominent in Site 1A and include contributions from ten residues: Gln10, Phe13, Ala14, Thr124, Val127, Val128, Met216, Ser220, Gln222, and Leu227. Electrostatic interactions are relatively few; the sulfonate and benzimidazole groups form hydrogen bonds with Asn230.

Pose 1B of **4** is observed in only two of the five chains in the asymmetric unit. The electron density for this pose is weaker than 1A and the occupancies refined to lower values of 0.69 and 0.76 (Figure 4A). Sites 1A and 1B are very close together. In fact, the phenyl ring of **4** in pose 1B contacts the benzimidazole group of **4** in pose 1A (Figure 4A, right panel). This aromatic stacking interaction apparently stabilizes the 1B pose, since we never observed the 1B pose in the absence of 1A. These results suggests that Site 1A is the higher affinity of the two sites for **4**. The sulfonate group binds at the N-terminus of αB, forming hydrogen bonds with the backbone of this helix (Ala40) and presumably stabilizing the helix dipole (Figure 4A).

The structure of PYCR1 complexed with **5** was determined at 1.5 Å resolution. **5** binds in Site 1A and has strong electron density in all five chains with refined occupancies of 0.63–0.75 (Figure 4B). Unlike **4**, compound **5** was not observed in Site 1B. The sulfonate group of **5** is shifted compared to **4**, enabling hydrogen bonds with Gln222 in addition to Asn230. Like **4**, nonpolar interactions are prominent, with Gln10, Phe13, Ala14, Thr124,

Val127, Val128, Met216, His219, Ser220, and Leu227 contacting the aromatic rings of **5**. The chlorine substituents of **5** make no halogen bonds with PYCR1.

Poses and interactions of compounds 9 and 10 in allosteric Site 2

Compound **9** binds in allosteric Site 2 (Figure 3E). Convincing electron density for the compound was observed in all five chains in the asymmetric unit with occupancies ranging from 0.59 to 0.66 (Figure 5A). **9** packs between αJ of one protomer and β8 of the Rossmann dinucleotide-binding domain of another protomer. The binding pocket is mainly hydrophobic. Phe158, Glu161, Pro198, Arg200, Leu201, and Arg204 contribute nonpolar interactions, primarily with the phenyl group of **9**. A few electrostatic interactions are also observed. Arg200 wraps over one edge of the inhibitor, forming cation-π interactions, while Thr160 hydrogen bonds with the amine group of **9**. The sulfonate and carbonyl groups of the inhibitor form hydrogen bonds with water molecules but do not interact directly with the enzyme; one of the water molecules bridges the sulfonate to the backbone of Arg200 (Supplementary Figure S2).

Compound **10** also binds in Site 2. The electron density for **10** was relatively weak and supported modeling of the inhibitor at low occupancy (0.49) in only one of the five chains of the asymmetric unit (Figure 5B). As with **9**, most of the interactions of **10** with the enzyme are nonpolar and involve Thr160, Glu161, Val162, Leu166, Pro198, Arg200, Leu201, and Arg204. The cation-π interaction with Arg200 is also observed with **10**.

Validation of crystallographic hits with enzyme activity assays

Enzyme activity assays were used to determine whether the remote binders inhibit PYCR1. The activity of PYCR1 was measured as a function of compound concentration (0–5 mM) with NAD(P)H and L-P5C fixed at 50 μM and 200 μM, respectively. Each compound showed concentration-dependent inhibition of PYCR1 (Figure 6). Regardless of the coenzyme, **9** showed the strongest inhibition followed by **10**, **4**, and **5**. Thus, the Site 2 binders appear to be better inhibitors than the Site 1 binders. The IC_{50} values of **9** are 2 μM and 8 μM when using NADPH and NADH, respectively (Table 3). Those of compound **10** are 10–20 times higher. The IC_{50} values of **4** are ~200 μM and ~500 μM, for NADPH and NADH, respectively. Compound **5** is the weakest inhibitor with IC_{50} in the millimolar range. In all cases, the apparent inhibition was stronger when using NADPH. These results show that the remote binders inhibit enzymatic activity and thus are the first allosteric inhibitors of PYCR1.

PYCR1 enzyme activity was also measured in the presence of the inhibitor while varying the concentration of either L-P5C or NADH. Compounds **4** and **9** were used as representatives of inhibitors that bind to Sites 1 and 2, respectively. The data were fitted globally to a mixed model of inhibition (Equation 1) to yield the apparent inhibition parameters, K_i and α, where K_i refers to the inhibitor binding the free enzyme and αK_i represents binding to E-S complexes (Figure 7, Table 4). Consistent with the IC_{50} data, the assays show that **9** is a better inhibitor than **4**. Using L-P5C as the variable substrate, K_i and αK_i for **9** are 110 μM and 143 μM, respectively, compared to >1 mM for **4**. Similar results were obtained when

varying the NADH concentration; K_i and αK_i for **9** are 160 μM and 32 μM, compared to 1–2 mM for **4**. Thus, **9** is a 10-fold better inhibitor than **4** under the conditions used.

Quaternary complexes of PYCR1 with allosteric inhibitors, NADH, and proline analogs.

Quaternary complexes of PYCR1 with allosteric inhibitors and catalytically relevant ligands were determined to gain structural insight into the mechanism of inhibition. The kinetic mechanism of PYCR1 proceeds through a ternary enzyme-L-P5C-NAD(P)H complex in which the hydride transfer step occurs. Results described above show that compounds **4**, **5**, **9**, and **10** bind to the apo enzyme and inhibit enzymatic activity, yet none occupy the coenzyme- or L-P5C binding sites. We therefore asked whether the allosteric inhibitors can also bind to the catalytically essential ternary complex. Co-crystallization and crystal soaking trials were performed with various combinations of an allosteric inhibitor, NADH, and one of two proline analogs, either (2S)-2-hydroxy-3,3-dimethylbutanoic acid (PDB ligand ID G8I) or S-(−)-tetrahydro-2-furoic acid (THFA). Both proline analogs are known inhibitors of PYCR1 that bind in the L-P5C site (28, 30). These experiments resulted in 1.8 Å resolution crystal structures of three quaternary complexes: PYCR1-**9**-NADH-G8I, PYCR1-**10**-NADH-G8I, and PYCR1-**4**-NADH-THFA (Table 2).

The quaternary complexes suggest that the mechanism of inhibition results from the compounds binding to both the apo enzyme and the ternary catalytic complex. The binding locations and poses of the allosteric inhibitors in the quaternary complexes are nearly identical to those in the binary complexes. The density for **4** was weaker in the quaternary complex than in the binary complex; **4** was modeled into Site 1A in two chains at occupancies of 0.68 and 0.72 (Figure 8A). Electron density for **4** in Site 1B was not observed. Interestingly, stronger electron density was obtained for **9** and **10** in the quaternary complexes compared to the binary ones. Both **9** and **10** could be modeled in all five chains of the quaternary complexes with occupancies of 0.77 – 0.85 for **9** and 0.60 – 0.69 for **10** (Figure 8B, 8C). In two of the chains, **10** is modeled in two conformations, which differ in the orientation of the amide group. The electron density for NADH and the proline analogs was strong and supported modeling of these ligands in all five chains at high occupancy (Figure 8).

The quaternary complexes confirm the interpretation of the binary complex structures that the allosteric inhibitor binding sites do not overlap those of L-P5C and NAD(P)H. In all the quaternary complexes, the proline analog and NADH adopt their expected poses. NADH binds to the Rossmann fold domain in an extended conformation in which the nicotinamide group is next to the proline analog (Figure 8). Compound **4** is near the nicotinamide of NADH, whereas **9** and **10** approach the AMP group from the opposite side of the coenzyme. The benzimidazole group of **4** is 7 Å from the amide group of NADH; however, Asn230, Gln10, and Thr124 block the intervening space (Figure 8A). The sulfonate groups of **9** and **10** are 7 Å from NADH and 13 Å from the proline analog; the path between these inhibitors and the active site ligands is not blocked by the protein (Figure 8B,8C). In summary, the quaternary complex structures suggest that **4**, **9**, and **10** can bind to the ternary PYCR1-L-P5C-NADH complex in addition to the free enzyme, consistent with the kinetic data following a mixed model of inhibition.

Ternary complex of PYCR1 with 5 and the proline analog G8I: Promiscuous binding of 5 to both allosteric sites and the active site

A 1.75 Å structure of the ternary complex of PYCR1 with **5** and G8I was determined from a crystal grown in the presence of both **5** (21 mM) and G8I (10 mM) and then soaked in 50 mM of **5** (Table 2). Unexpectedly, strong electron density for the inhibitor was observed not only in allosteric Site 1A, but also in allosteric Site 2 and the NAD(P)H binding site (Figure 9A). **5** was modeled into Site 1A in all five chains with occupancies of 0.62–73, which is similar to the occupancies of **5** in the binary complex (pdb_00009p0r). The pose and interactions of **5** in Site 1A are like those in the binary complex (Figure 9A, left inset). **5** was also modeled into Site 2 in two chains (Q = 0.65, 0.73). **5** in Site 2 mimics **9**/**10** by forming a cation-**π** interaction with Arg200 (Figure 9A, middle inset). Finally, **5** was modeled in the NAD(P)H site in two chains (Q = 0.64 0.76) (Figure 9A, right inset).

Compound **5** in the NAD(P)H binding site mimics the coenzyme. The resemblance can be seen in a superposition of the active sites of the ternary PYCR1-**5**-G8I complex and the quaternary PYCR1-**9**-NADH-G8I complex (Figure 9B). **5** occupies the space reserved for the nicotinamide mononucleotide part of the coenzyme. The dichlorobenzene of **5** aligns almost perfectly with the nicotinamide ring, while the sulfonate docks into the coenzyme pyrophosphate site (Figure 9B, left panel). Like the nicotinamide ring of NAD(P)H, the dichlorobenzene is flanked by the sidechain of Leu11 and the t-butyl group of G8I (Figure 9B, right panel). Similar to the pyrophosphate of NAD(P)H, the sulfonate of **5** binds at the N-terminus of the first helix of the Rossmann fold domain (αA) and forms hydrogen bonds with Gln10 and Leu11.

Discussion

We serendipitously discovered the first allosteric inhibitors of PYCR1. The compounds screened contained carboxylic acid isosteres that were assumed to bind in the αK-αL loop of the active site, based on similarity to known PYCR1 inhibitors from Meeks et al. (22) and docking. Notably, ten of the compounds feature the sulfonate group, which is known to target the αK-αL loop, based on the structures of PYCR1 complexed with small sulfonate-anchored compounds (21, 30) (pdb_00008tdb, pdb_00009rzz). We therefore expected the sulfonate compounds to bind in the active site, but only compound **8** bound as anticipated. However, four other sulfonate compounds were found to bind at remote sites located in the oligomer interface of the PYCR1 decamer. Although these binding events were unexpected, it is likely due to the small, fragment-like size of the compounds and the structural complexity of the PYCR1 decamer. Thus, this screening yielded two important findings. First, it confirmed a previously observed structure–activity relationship for PYCR1 inhibitors among carboxylic acids. Like two of the inhibitors from Meeks et al. (22), **8** consists of a bicyclic ring system with an amide group in the ring distal from the anionic anchor. Although **12** and **13** also fit this SAR profile (Figure 2), they were not hits, indicating that sulfonamide and nitro are not suitable replacements for carboxylate. The second finding is that the use of fragment-like compounds bearing sulfonic acid functional groups enabled the identification of novel binding sites, offering a new perspective for PYCR1 inhibition strategies.

All four remote binders inhibited PYCR1 enzymatic activity, with **9** showing the strongest inhibition characterized by the mixed inhibition parameters K_i = 110 μM, αK_i = 143 μM when L-P5C was varied, and K_i = 160 μM, αK_i = 32 μM when NADH was varied. Although the strength of inhibition might be considered modest to weak compared to drug-like leads, the fact that *any* inhibition was observed is notable considering that they are relatively small compounds in the molecular weight range typical for fragments. For reference, fragment hits commonly have affinities in the range of 10 mM to 10 μM (31, 32). Indeed, several hits from previous PYCR1 crystallographic fragment screening campaigns showed no apparent enzyme inhibition (21, 22). Thus, it is encouraging that all four remote binders inhibit PYCR1 enzyme activity, and furthermore the inhibition parameters of **9** (32–160 μM) are on the high affinity end of the spectrum of hits from crystallographic fragment screening.

Allosteric inhibitors are valued in drug discovery. Allostery represents one of the most powerful mechanisms for modulating protein function. Targeting allosteric sites can provide higher selectivity and fewer side effects compared to orthosteric drugs (33). Allosteric pockets are recognized as new avenues to overcome resistance and heterogeneity in cancer (34) and may lead to therapeutic routes for “undruggable” targets (33). Targeting the allosteric groove of PYCR1 may enable the development inhibitors with specificity for PYCR1 over the related enzymes PYCR2 and PYCR3.

The mechanisms of the allosteric inhibitors of PYCR1 are likely complex and will require more work to elucidate; however, the current data provide initial insight. The crystal structures of the binary complexes show that all four compounds can bind to the apo enzyme; however, the purely competitive mechanism is unlikely because none of the allosteric inhibitors overlap the NAD(P)H or L-P5C binding sites. Further, **4**, **9**, and **10** likely also bind to the PYCR1-L-P5C NADH ternary complex, based on the crystal structures of the enzyme complexed with an allosteric inhibitor, NADH, and a proline analog. The mixed inhibition model provided the best fit to the kinetic data, consistent with the inhibitors binding more than one form of the enzyme, i.e., the free enzyme and E-S complexes. Finally, the number of allosteric sites occupied per decamer ranged from 2 to 10, raising the possibility of cooperativity of binding, which would add complexity to the mechanism of inhibition.

The allosteric inhibitors are novel in that the anionic group appears to be a spectator rather than an anchor. In all other structurally validated PYCR1 inhibitors, the anionic group – either carboxylate or sulfonate – packs tightly into the αK-αL loop where it forms several hydrogen bonds. For example, carboxylate anchors typically form 4–5 hydrogen bonds with the αK-αL loop, whereas the sulfonate of 1-hydroxyethane-1-sulfonate (pdb_00008tdb) interacts more extensively with the loop, forming 7 hydrogen bonds. In contrast, the sulfonate groups of the allosteric inhibitors make relatively few hydrogen bonds with the enzyme. The sulfonates of **9** and **10** form hydrogen bonds with water molecules but do not directly interact with the enzyme. Those of **4** and **5** make only 2–3 hydrogen bonds. Correspondingly, the sulfonate groups of the allosteric inhibitors exhibit relatively high solvent exposure compared to the anionic anchors bind in the αK-αL loop (Figures 4 and 5, right panels). Thus, it appears that the sulfonates of the allosteric inhibitors play a more passive role in mediating association with the enzyme, and nonpolar interactions dominate

the interaction interface. These observations suggest that it may be possible to replace the sulfonate with other moieties to increase the interactions with the enzyme.

The serendipitous discovery of the allosteric groove enables new strategies for PYCR1 inhibitor development. The groove provides vacant space to accommodate larger analogs or to grow the present compounds to increase interactions with the enzyme (Figure 10). A linking-like approach may be realized with larger analogs of **4** and **5** that span Sites 1A and 1B. Analogs of **9** and **10** with groups that invade the NAD(P)H site could be dualsteric inhibitors (35). The proximity of the **9** and **10** to NADH (7 Å) implies feasibility of dualsteric strategies (Figure 8B,C). We expect our work to herald a new era of PYCR1 inhibitor design.

Materials and methods

Docking

A set of fragment-like carboxylic acid bioisosteres was extracted from the Enamine In-Stock collection using substructure searches, yielding 319 compounds. In parallel, a set of fragment-like sulfonic acids was selected from the same collection, resulting in 1,200 compounds.

Docking was performed following the procedure described previously (22) using ICM Pro by Molsoft. For the carboxylic acid bioisostere fragments, new docking templates were prepared to enable proper positioning of these fragments within the specific sub-pocket targeted by the bioisostere moiety. For virtual screening of the sulfonic acid set, a newly generated docking grid was used based on the PYCR1 structure (pdb_00008tdb), which contains a sulfonic acid-based PYCR1 inhibitor (30). Examples of the docking boxes are shown in Supplementary Figure S3.

Based on docking scores and visual inspection of binding modes, 22 compounds were selected for experimental testing against PYCR1. These compounds were sourced through Chemspace. SMILES strings and Chemspace IDs are provided in Supplementary Table S1, while selected physicochemical properties (molecular weight, number of heavy atoms, and logP) are listed in Supplementary Table S2.

Co-crystallization of PYCR1-inhibitor complexes

PYCR1 was purified as described previously (22, 30). For the screening by X-ray crystallography, each compound was co-crystallized with PYCR1. Stock solutions of **2**-**11** and **14**-**22** were made in aqueous buffer containing Tris pH 8.5. The other compounds were less soluble in this buffer and were instead dissolved in either 50% (w/v) PEG 3350 (**1**, **13**) or 100% DMSO (**12**). Prior to crystallization, the stock solutions were combined with PYCR1 so that the enzyme concentration was 10 mg/mL and the compound concentration was 25 mM, except for **1** (11 mM), **12** (1 mM), **13** (12.5 mM), and **20** (15 mM). Crystals were grown in sitting drops using a reservoir solution of 0.34–0.4M Li_2SO_4, 0.1M HEPES pH 7.5, and 17–22% (w/v) PEG 3350. Sitting drops were made by combining 2 μL of reservoir solution with 2 μL of protein-ligand solution. Drops were seed-streaked with PYCR1 microcrystals. Crystals were prepared for cryogenic data collection by soaking in

a solution containing no Li_2SO_4, 0.1M HEPES pH 7.5, 22% (w/v) PEG 3350, and 20% (v/v) PEG 200, plus additional compound and then flash-cooled in liquid nitrogen. We note that exclusion of Li_2SO_4 from the cryobuffer helped to lower the occupancy of sulfate ion in the active site. The compound concentration in the cryobuffer was 50 mM for **2**-**11** and **14**-**22**, 11 mM for **1**, 19 mM for **12**, and 25 mM for **13**. Two X-ray diffraction data sets were collected for each compound except **15** and **21**, for which only one data set was obtained. In total, 87 data sets were collected with an average resolution of 1.7 ± 0.2 Å. To improve the occupancies of **9** and **10** observed in the initial round of structures, additional crystals were soaked with 125 mM of **9** or 100 mM of **10**.

Following analysis of the results from the initial X-ray crystallography screening of the library, crystals of quaternary and ternary complexes of PYCR1 with a hit compound and combinations of NADH and a proline analog were prepared. PYCR1 was co-crystallized with **9** (12 mM), NADH (3.5 mM), and the proline analog inhibitor (2S)-2-hydroxy-3,3-dimethylbutanoic acid (PDB ligand ID G8I) (10 mM) to form a quaternary PYCR1-**9**-NADH-G8I complex; the cryobuffer for this crystal included 125 mM of **9**. The quaternary PYCR1-**10**-NADH-G8I complex was prepared similarly; PYCR1 was co-crystallized with **10** (20 mM), NADH (3.5 mM), and G8I (10 mM). The cryobuffer for this crystal included 88 mM of **10** and 15 mM of G8I. The quaternary complex with **4**, NADH, and the proline analog inhibitor S-(−)-tetrahydro-2-furoic acid (THFA) was also prepared. PYCR1 was co-crystallized with **4** (7 mM), NADH (3.5 mM), and THFA (10 mM); the cryobuffer for this crystal included 44 mM of **4** and 15 mm of THFA. Finally, crystals of a ternary complex of PYCR1 with **5** and G8I were obtained. PYCR1 was co-crystallized with **5** (21 mM) and G8I (10 mM), and the cryobuffer contained 50 mM of **5**.

X-ray crystal structure determination

Shutterless X-ray diffraction data were collected at the Advanced Light Source using beamline 8.2.1 and the Advanced Photon Source using beamline 24-ID-E. The data were processed with XDS (36) and Aimless (37) through the automated pipeline of the beamline. The space group is *C*2 with five molecules in the asymmetric unit arranged as one-half of a pentamer-of-dimers decamer (2.5 dimers). X-ray diffraction data processing statistics are listed in Tables 1 and 2.

Initial phases were calculated by Fourier synthesis using a model derived from pdb_00008tcx. Iterative cycles of refinement and model building were performed with Phenix (38) and Coot (39). The *B*-factor model consisted of one TLS group per protein chain and isotropic *B*-factors for all non-hydrogen atoms. The structures were validated using MolProbity and the wwPDB validation service (40, 41). LigPlot+ was used to calculate enzyme-ligand interactions (29). CNS was used to build the crystal lattice for the analysis of crystal contacts (42). Crystallographic refinement statistics are listed in Tables 1 and 2. The atomic coordinates and structure factor amplitudes for all structures have been deposited in the PDB under the accession codes listed in Tables 1 and 2.

Enzyme inhibition assays

Enzyme activity measurements were performed using a BioTek Epoch 2 microplate spectrophotometer in Corning 96-well plates at 25 °C. The assay buffer contained 50 mM HEPES pH 7.5 and 1 mM EDTA. The decrease in absorbance at 340 nm was monitored and corresponds to the consumption of NAD(P)H in the reaction. A stock solution of D,L-P5C was diluted with 1 M Tris pH 8.5 and neutralized to pH 7–9 by dropwise addition of 6 M NaOH. The concentration of L-P5C was assumed to be half of the D,L-P5C stock.

For IC_{50} determination, the relative activity of PYCR1 was measured in the presence of variable inhibitor concentrations, with L-P5C and NAD(P)H present at 200 μM and 50 μM, respectively. The final concentration of PYCR1 was 10 nM. The microplate procedure was as follows. First, aliquots (10 μL) of the inhibitor solutions were added to the plate. Then, 40 μL of 1 mM L-P5C was added to each well via repeater pipette. Lastly, 150 μL of master mix containing PYCR1, NAD(P)H, and buffer including 50 mM HEPES pH 7.5 and 1 mM EDTA was added via a multichannel pipet to start the reaction. Each compound was tested in triplicate. A negative control (no inhibitor) was included in which water replaced the compound. Initial velocities were determined by linear regression of the first 5 min of absorbance data. The initial rates were converted to units of μM/s using the negative value of the slope and the extinction coefficient of NAD(P)H at 340 nm of 6220 M^{-1} cm^{-1}. The negative control reactions (no inhibitor) were averaged and used to normalize the rates in the presence of a compound. The data were fitted using Origin software to the generalized dose–response function for enzyme inhibition (equation 8.25 of Copeland (43)).

To study the kinetic mechanism of inhibition, activity assays were performed with either L-P5C or NADH as the variable substrate at multiple fixed inhibitor concentrations. When L-P5C was varied, NADH was fixed at 175 μM. When NADH was varied, L-P5C was fixed at 400 μM. The final concentration of PYCR1 was 7.5 nM. The microplate procedure was as follows. First, 10 μl of inhibitor solution was added to the plate. Then, the varied substrate was added to the plate, either 40 μl for L-P5C or 10 μl for NADH. Lastly, the remaining assay components (enzyme, fixed substrate) were added via a multichannel pipette to start the reaction. The total assay volume after adding all components was 200 μL. The initial rate data were fitted globally to the mixed model (Equation 1) using Origin software. During global fitting, V_{max}, K_m, K_i, and α were shared variables.

$$v = \frac{V_{max}[S]}{[S]\left(1 + \frac{[I]}{\alpha K_i}\right) + K_m\left(1 + \frac{[I]}{K_i}\right)} \quad (1)$$

Supplementary Material

Refer to Web version on PubMed Central for supplementary material.

Acknowledgements

We thank Jonathan Schuerman for help with X-ray diffraction data collection and processing at the Northeastern Collaborative Access Team beamlines. We thank Oseeyi Daudu from the Becker lab at University of Nebraska

for supplying D,L-P5C. Beamline 8.2.1 of the Advanced Light Source, a DOE Office of Science User Facility under Contract No. DE-AC02-05CH11231, is supported in part by the ALS-ENABLE program funded by the National Institutes of Health, National Institute of General Medical Sciences, grant P30 GM124169-01. This work is based upon research conducted at the Northeastern Collaborative Access Team beamlines, which are funded by the National Institute of General Medical Sciences from the National Institutes of Health (P30 GM124165). The Eiger 16M detector on the 24-ID-E beam line is funded by a NIH-ORIP HEI grant (S10OD021527). This research used resources of the Advanced Photon Source, a U.S. Department of Energy (DOE) Office of Science User Facility operated for the DOE Office of Science by Argonne National Laboratory under Contract No. DE-AC02-06CH11357.

Funding Information

Research reported in this publication was supported by the National Institute of General Medical Sciences of the National Institutes of Health under award number R01GM132640. K.R.M. was supported in part by a Wayne L. Ryan Fellowship through the Ryan Foundation.

Data availability

Materials from this study will be made available from the corresponding author upon reasonable request. Atomic coordinates and structure factor amplitudes have been deposited in the PDB under accession codes: pdb_00009p0q (44), pdb_00009p0r (45), pdb_00009p0s (46), pdb_00009p0u (47), pdb_00009p0t (48), pdb_00009p0v (49), pdb_00009q45 (50), pdb_00009q46 (51).

Abbreviations:

G8I	(2S)-2-hydroxy-3,3-dimethylbutanoic acid
NFLP	N-formyl-L-proline
P5C	Δ^1-pyrroline-5-carboxylate
PYCR1	Δ^1-pyrroline-5-carboxylate reductase 1
THFA	S-(-)-tetrahydro-2-furoic acid

References

1. Bergers G and Fendt SM (2021) The metabolism of cancer cells during metastasis. Nat Rev Cancer. 21, 162–180. 10.1038/s41568-020-00320-2 [PubMed: 33462499]
2. Tanner JJ, Fendt SM and Becker DF (2018) The Proline Cycle As a Potential Cancer Therapy Target. Biochemistry. 57, 3433–3444. 10.1021/acs.biochem.8b00215 [PubMed: 29648801]
3. Burke L, Guterman I, Palacios Gallego R, Britton RG, Burschowsky D, Tufarelli C et al. (2020) The Janus-like role of proline metabolism in cancer. Cell Death Discov. 6, 104. 10.1038/s41420-020-00341-8 [PubMed: 33083024]
4. Bogner AN, Stiers KM and Tanner JJ (2021) Structure, biochemistry, and gene expression patterns of the proline biosynthetic enzyme pyrroline-5-carboxylate reductase (PYCR), an emerging cancer therapy target. Amino Acids. 53, 1817–1834. 10.1007/s00726-021-02999-5 [PubMed: 34003320]
5. Phang JM (2021) Perspectives, past, present and future: the proline cycle/proline-collagen regulatory axis. Amino Acids. 53, 1967–1975. 10.1007/s00726-021-03103-7 [PubMed: 34825974]
6. D'Aniello C, Patriarca EJ, Phang JM and Minchiotti G (2020) Proline Metabolism in Tumor Growth and Metastatic Progression. Front Oncol. 10, 776. 10.3389/fonc.2020.00776 [PubMed: 32500033]
7. Ding Z, Ericksen RE, Lee QY and Han W (2021) Reprogramming of mitochondrial proline metabolism promotes liver tumorigenesis. Amino Acids. 10.1007/s00726-021-02961-5

8. Li Y, Bie J, Song C, Liu M and Luo J (2021) PYCR, a key enzyme in proline metabolism, functions in tumorigenesis. Amino Acids. 53, 1841–1850. 10.1007/s00726-021-03047-y [PubMed: 34273023]
9. Li Y, Xu J, Bao P, Wei Z, Pan L, Zhou J et al. (2022) Survival and clinicopathological significance of PYCR1 expression in cancer: A meta-analysis. Front Oncol. 12, 985613. 10.3389/fonc.2022.985613 [PubMed: 36119513]
10. Harb OA, Elfeky MA, Alabiad MA, Hemeda R, Allam AS, El Hawary AT et al. (2024) PYCR1, BANF1, and STARD8 Expression in Gastric Carcinoma: A Clinicopathologic, Prognostic, and Immunohistochemical Study. Appl Immunohistochem Mol Morphol. 32, 102–110. 10.1097/PAI.0000000000001173 [PubMed: 37982568]
11. Zhang M, Bi B, Liu G and Fan X (2024) PYCR1 expresses in cancer-associated fibroblasts and accelerates the progression of C6 glioblastoma. Histol Histopathol. 18762. 10.14670/HH-18-762
12. Liu K, Yang X, Tang X and Tang B (2025) The transcription factor FOXA1 upregulates PYCR1-mediated autophagy to suppress antitumor immunity in lung adenocarcinoma. Cancer Immunol Immunother. 74, 290. 10.1007/s00262-025-04144-7 [PubMed: 40848149]
13. Wang H, Xu M, Zhang T, Pan J, Li C, Pan B et al. (2024) PYCR1 promotes liver cancer cell growth and metastasis by regulating IRS1 expression through lactylation modification. Clin Transl Med. 14, e70045. 10.1002/ctm2.70045 [PubMed: 39422696]
14. Guo P, Wu C, Wang T, Song Y, Liu X, Wang X et al. (2025) The key enzyme PYCR1 in proline metabolism: a dual driver of cancer progression and fibrotic remodeling. J Enzyme Inhib Med Chem. 40, 2545620. 10.1080/14756366.2025.2545620 [PubMed: 40891362]
15. You C, He J, Cao C, Sheng D, Wang L, Huang Z et al. (2024) PYCR1 regulates TRAIL-resistance in non-small cell lung cancer cells by regulating the redistribution of death receptors. Oncology Letters. 27. 10.3892/ol.2024.14349
16. Kay EJ, Zanivan S and Rufini A (2023) Proline metabolism shapes the tumor microenvironment: from collagen deposition to immune evasion. Current Opinion in Biotechnology. 84. 10.1016/j.copbio.2023.103011
17. Meng YQ, Feng HM, Li B, Xie Y, Li Z, Li ZQ et al. (2025) PYCR1 Promotes Esophageal Squamous Cell Carcinoma by Interacting With EGFR to Affecting the PI3K/Akt/mTOR Signaling Pathway. J Gene Med. 27, e70017. 10.1002/jgm.70017 [PubMed: 40102683]
18. Li Z, Jiang Q, Yang Q, Zhou Y and Wang J (2025) Hypoxia-induced PYCR1 regulates glycolysis and histone lactylation to promote bladder cancer progression and metastasis via SLC6A14/Glutamine metabolism. Cancer Biol Ther. 26, 2546219. 10.1080/15384047.2025.2546219 [PubMed: 40808274]
19. Meeks KR, Bogner AN, Nix JC and Tanner JJ (2024) Crystallographic Fragment Screening of a Bifunctional Proline Catabolic Enzyme Reveals New Inhibitor Templates for Proline Dehydrogenase and L-Glutamate-γ-semialdehyde Dehydrogenase. Molecules. 29, 5408. [PubMed: 39598797]
20. Christensen EM, Bogner AN, Vandekeere A, Tam GS, Patel SM, Becker DF et al. (2020) In crystallo screening for proline analog inhibitors of the proline cycle enzyme PYCR1. J Biol Chem. 295, 18316–18327. 10.1074/jbc.RA120.016106 [PubMed: 33109600]
21. Ragin-Oh W, Czerwonka D, Tran LH, Forlani G and Ruszkowski M (2025) Crystallographic fragment screening reveals new starting points for PYCR1 inhibitor design. Bioorg Chem. 165, 109024. 10.1016/j.bioorg.2025.109024 [PubMed: 41016381]
22. Meeks KR, Ji J, Protopopov MV, Tarkhanova OO, Moroz YS and Tanner JJ (2024) Novel Fragment Inhibitors of PYCR1 from Docking-Guided X-ray Crystallography. J Chem Inf Model. 64, 1704–1718. 10.1021/acs.jcim.3c01879 [PubMed: 38411104]
23. Bredael K, Geurs S, Clarisse D, De Bosscher K and D'Hooghe M (2022) Carboxylic Acid Bioisosteres in Medicinal Chemistry: Synthesis and Properties. In: Journal of Chemistry. Hindawi Limited,
24. Kalgutkar AS and Daniels JS (2010) Carboxylic acids and their bioisosteres In: Metabolism, pharmacokinetics and toxicity of functional groups: Impact of chemical building blocks on admet. p. 99–167.

25. Ballatore C, Huryn DM and Smith AB 3rd (2013) Carboxylic acid (bio)isosteres in drug design. ChemMedChem. 8, 385–395. 10.1002/cmdc.201200585 [PubMed: 23361977]
26. Lassalas P, Gay B, Lasfargeas C, James MJ, Tran V, Vijayendran KG et al. (2016) Structure Property Relationships of Carboxylic Acid Isosteres. Journal of Medicinal Chemistry. 59, 3183–3203. 10.1021/acs.jmedchem.5b01963 [PubMed: 26967507]
27. Verma A, Waiker DK, Gupta PS, Kumar M and Shrivastava SK (2025) Bioisosterism: an approach to develop new anti-cancer agents. Eur J Med Chem. 300, 118166. 10.1016/j.ejmech.2025.118166 [PubMed: 40975008]
28. Christensen EM, Patel SM, Korasick DA, Campbell AC, Krause KL, Becker DF et al. (2017) Resolving the cofactor-binding site in the proline biosynthetic enzyme human pyrroline-5-carboxylate reductase 1. J Biol Chem. 292, 7233–7243. 10.1074/jbc.M117.780288 [PubMed: 28258219]
29. Laskowski RA and Swindells MB (2011) LigPlot+: Multiple ligand-protein interaction diagrams for drug discovery. Journal of Chemical Information and Modeling. 51, 2778–2786. 10.1021/ci200227u [PubMed: 21919503]
30. Meeks KR, Bogner AN and Tanner JJ (2024) Screening a knowledge-based library of low molecular weight compounds against the proline biosynthetic enzyme 1-pyrroline-5-carboxylate 1 (PYCR1). Protein Sci. 33, e5072. 10.1002/pro.5072 [PubMed: 39133178]
31. Hopkins AL, Keseru GM, Leeson PD, Rees DC and Reynolds CH (2014) The role of ligand efficiency metrics in drug discovery. Nat Rev Drug Discov. 13, 105–121. 10.1038/nrd4163 [PubMed: 24481311]
32. Scott DE, Coyne AG, Hudson SA and Abell C (2012) Fragment-based approaches in drug discovery and chemical biology. Biochemistry. 51, 4990–5003. 10.1021/bi3005126 [PubMed: 22697260]
33. Lu S, Li S and Zhang J (2014) Harnessing allostery: a novel approach to drug discovery. Med Res Rev. 34, 1242–1285. 10.1002/med.21317 [PubMed: 24827416]
34. Nussinov R, Yavuz BR and Jang H (2025) Allostery in Disease: Anticancer Drugs, Pockets, and the Tumor Heterogeneity Challenge. J Mol Biol. 437, 169050. 10.1016/j.jmb.2025.169050 [PubMed: 40021049]
35. Li N, Zheng G, Fu L, Liu N, Chen T and Lu S (2024) Designed dualsteric modulators: A novel route for drug discovery. Drug Discov Today. 29, 104141. 10.1016/j.drudis.2024.104141 [PubMed: 39168404]
36. Kabsch W (2010) XDS. Acta Crystallogr D Biol Crystallogr. 66, 125–132. S0907444909047337 [pii] 10.1107/S0907444909047337 [PubMed: 20124692]
37. Evans PR and Murshudov GN (2013) How good are my data and what is the resolution? Acta Crystallogr D Biol Crystallogr. 69, 1204–1214. 10.1107/S0907444913000061 [PubMed: 23793146]
38. Afonine PV, Grosse-Kunstleve RW, Echols N, Headd JJ, Moriarty NW, Mustyakimov M et al. (2012) Towards automated crystallographic structure refinement with phenix.refine. Acta Crystallogr D Biol Crystallogr. 68, 352–367. 10.1107/S0907444912001308 [PubMed: 22505256]
39. Emsley P, Lohkamp B, Scott WG and Cowtan K (2010) Features and development of Coot. Acta Crystallogr D Biol Crystallogr. 66, 486–501. 10.1107/S0907444910007493 [PubMed: 20383002]
40. Chen VB, Arendall WB 3rd, Headd JJ, Keedy DA, Immormino RM, Kapral GJ et al. (2010) MolProbity: all-atom structure validation for macromolecular crystallography. Acta Crystallogr D Biol Crystallogr. D66, 12–21. 10.1107/S0907444909042073
41. Gore S, Sanz Garcia E, Hendrickx PMS, Gutmanas A, Westbrook JD, Yang H et al. (2017) Validation of Structures in the Protein Data Bank. Structure. 25, 1916–1927. 10.1016/j.str.2017.10.009 [PubMed: 29174494]
42. Brunger AT (2007) Version 1.2 of the Crystallography and NMR system. Nat Protoc. 2, 2728–2733. 10.1038/nprot.2007.406 [PubMed: 18007608]
43. Copeland RA (2000) Enzymes: A Practical Introduction to Structure, Mechanism, and Data Analysis 2nd ed. Wiley-VCH, New York
44. Meeks KR, Mattingly CJ, Nix JC, Chuk O, Protopopov MV, Tarkhanova OO et al. (2025) Serendipitous discovery of an allosteric inhibitor binding groove in the proline

biosynthetic enzyme pyrroline-5-carboxylate reductase 1 (PYCR1) [Protein Data Bank (RCSB pdb_00009p0q)].

45. Meeks KR, Mattingly CJ, Nix JC, Chuk O, Protopopov MV, Tarkhanova OO et al. (2025) Serendipitous discovery of an allosteric inhibitor binding groove in the proline biosynthetic enzyme pyrroline-5-carboxylate reductase 1 (PYCR1) [Protein Data Bank (RCSB pdb_00009p0r)].
46. Meeks KR, Mattingly CJ, Nix JC, Chuk O, Protopopov MV, Tarkhanova OO et al. (2025) Serendipitous discovery of an allosteric inhibitor binding groove in the proline biosynthetic enzyme pyrroline-5-carboxylate reductase 1 (PYCR1) [Protein Data Bank (RCSB pdb_00009p0s)].
47. Meeks KR, Mattingly CJ, Nix JC, Chuk O, Protopopov MV, Tarkhanova OO et al. (2025) Serendipitous discovery of an allosteric inhibitor binding groove in the proline biosynthetic enzyme pyrroline-5-carboxylate reductase 1 (PYCR1) [Protein Data Bank (RCSB pdb_00009p0u)].
48. Meeks KR, Mattingly CJ, Nix JC, Chuk O, Protopopov MV, Tarkhanova OO et al. (2025) Serendipitous discovery of an allosteric inhibitor binding groove in the proline biosynthetic enzyme pyrroline-5-carboxylate reductase 1 (PYCR1) [Protein Data Bank (RCSB pdb_00009p0t)].
49. Meeks KR, Mattingly CJ, Nix JC, Chuk O, Protopopov MV, Tarkhanova OO et al. (2025) Serendipitous discovery of an allosteric inhibitor binding groove in the proline biosynthetic enzyme pyrroline-5-carboxylate reductase 1 (PYCR1) [Protein Data Bank (RCSB pdb_00009p0v)].
50. Meeks KR, Mattingly CJ, Nix JC, Chuk O, Protopopov MV, Tarkhanova OO et al. (2025) Serendipitous discovery of an allosteric inhibitor binding groove in the proline biosynthetic enzyme pyrroline-5-carboxylate reductase 1 (PYCR1) [Protein Data Bank (RCSB pdb_00009q45)].
51. Meeks KR, Mattingly CJ, Nix JC, Chuk O, Protopopov MV, Tarkhanova OO et al. (2025) Serendipitous discovery of an allosteric inhibitor binding groove in the proline biosynthetic enzyme pyrroline-5-carboxylate reductase 1 (PYCR1) [Protein Data Bank (RCSB pdb_00009q46)].

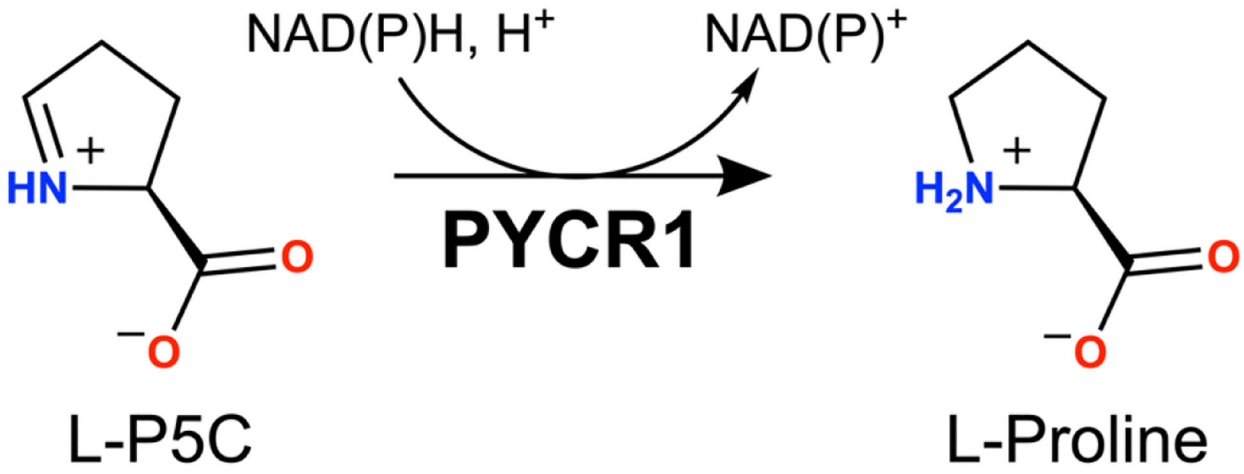

Figure 1.
Reaction catalyzed by PYCR1.

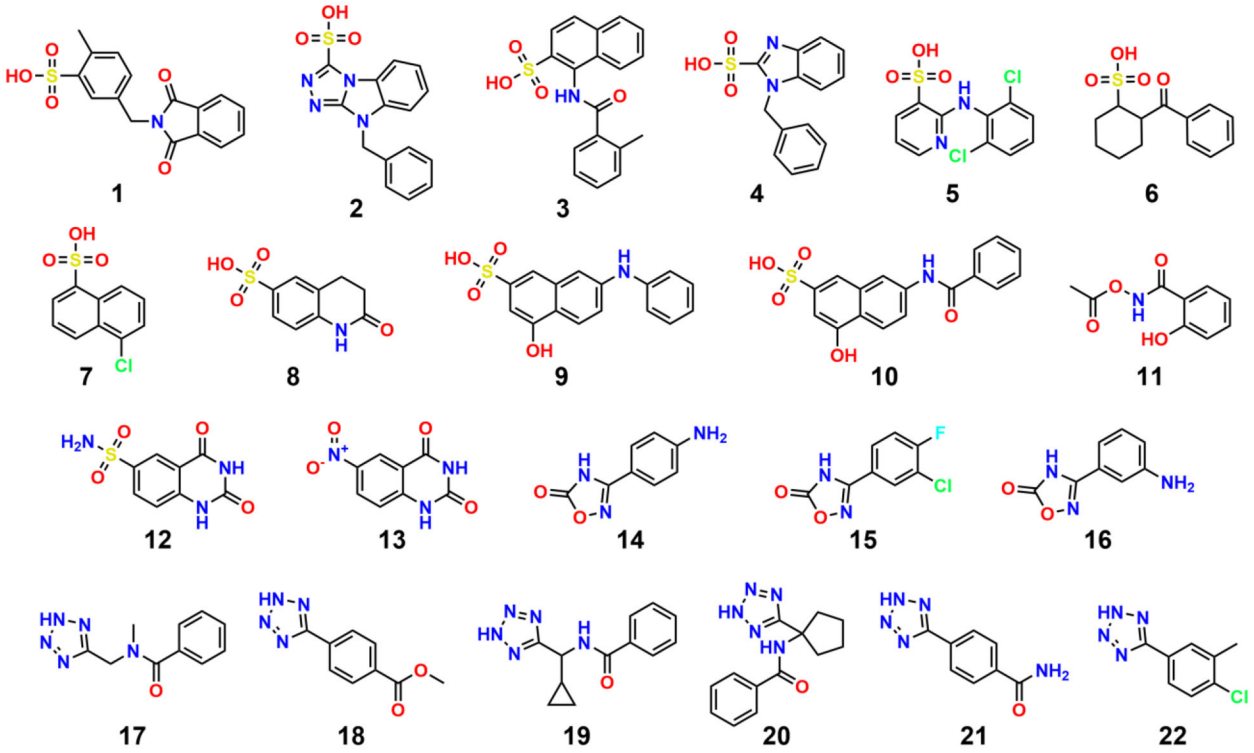

Figure 2.

Chemical structures of the carboxylic acid bioisosteres compound library. The bioisostere groups include sulfonic acid (**1** - **10**), hydroxamic acid (**11**), sulfonamide (**12**), nitro (**13**), 5-oxo-1,2,4-oxadiazole (**14** - **16**), and tetrazole (**17** - **22**).

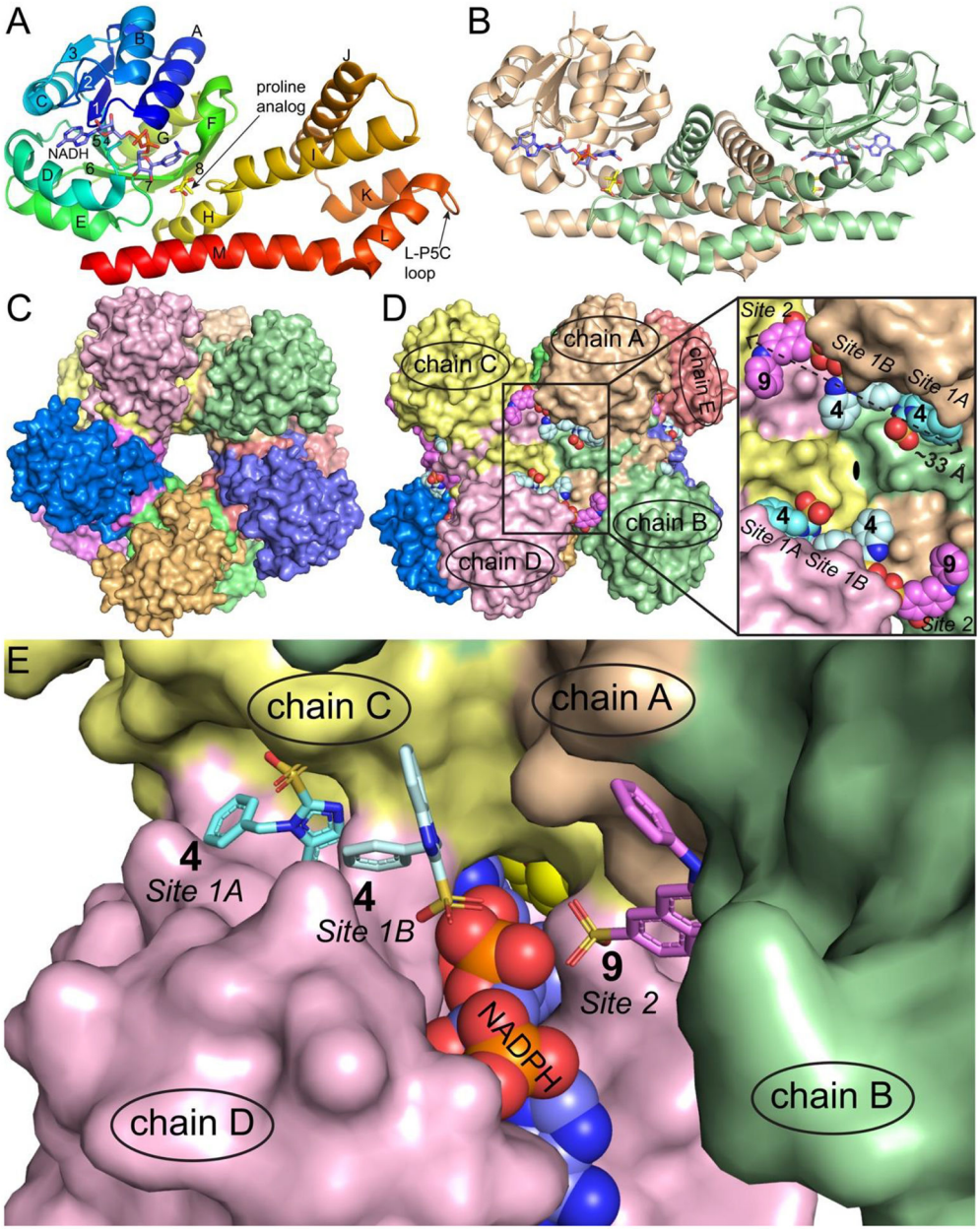

Figure 3.

Summary of PYCR1 structure and overview of the remote binding sites, as exemplified by compounds **4** and **9**. (A) The fold of PYCR1. The chain is colored in a rainbow scheme with blue at the N-terminus and red at the C-terminus. NADH (blue) and the proline analog (2S)-2-hydroxy-3,3-dimethylbutanoic acid (G8I, yellow) are shows in sticks. (B) The PYCR1 dimer. (C) The pentamer-of-dimers decamer of PYCR1 viewed down the 5-fold axis. Each protomer has a unique color. (D) Composite model of the decamer viewed down viewed down a 2-fold axis. Compounds **4** and **9** from pdb_00009p0q and pdb_00009p0s, respectively, have been mapped onto the structure to show the locations of the remote binding sites, which are labeled Site 1A, Site 1B, and Site 2. (E) Close-up view of the

remote binding sites for **4** and **9** showing their relationship to NAD(P)H. NADPH is from pdb_00005uav.

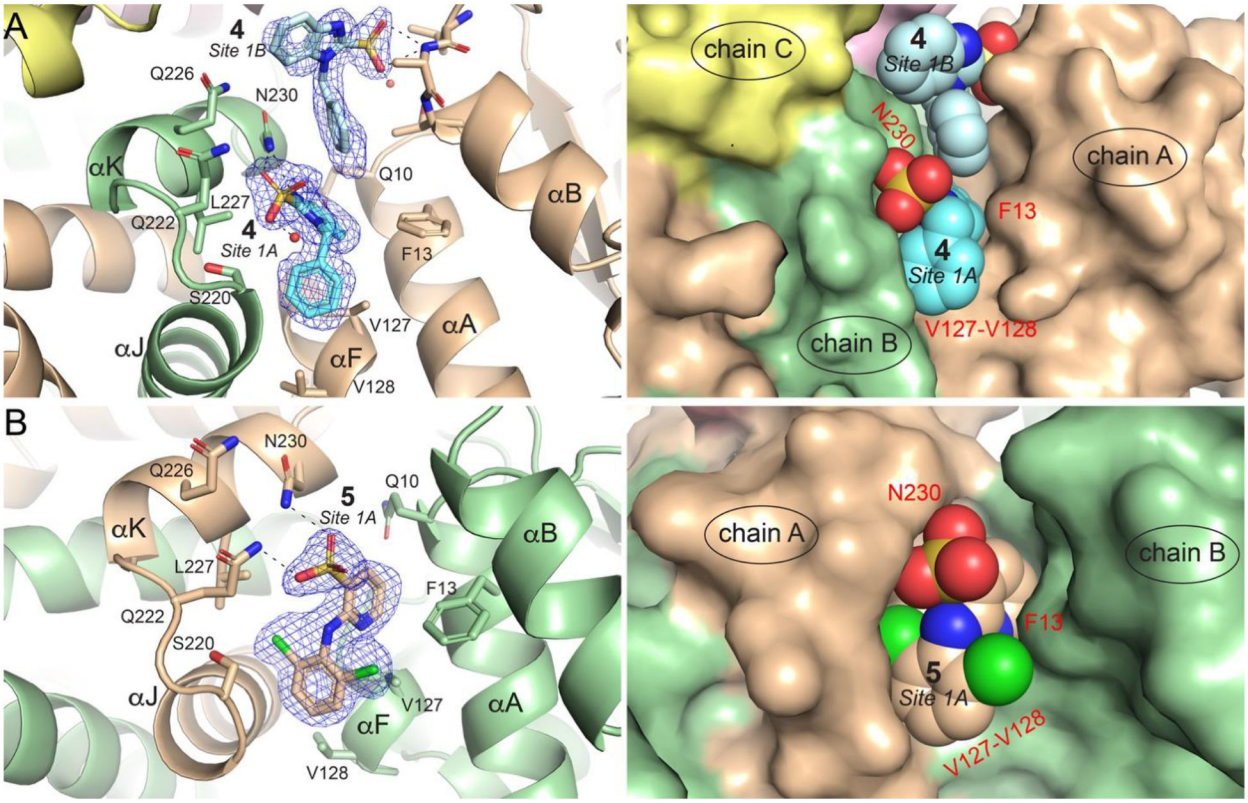

Figure 4.

The remote binding sites of compounds **4** and **5**. (A) Compound **4** in Sites 1A and 1B of the binary PYCR1-**4** complex (pdb_00009p0q). (B) Compound **5** in Site 1A of the binary PYCR1-**5** complex (pdb_00009p0r). In all panels, the mesh represents a polder map (4σ) and the chains of the decamer have different colors.

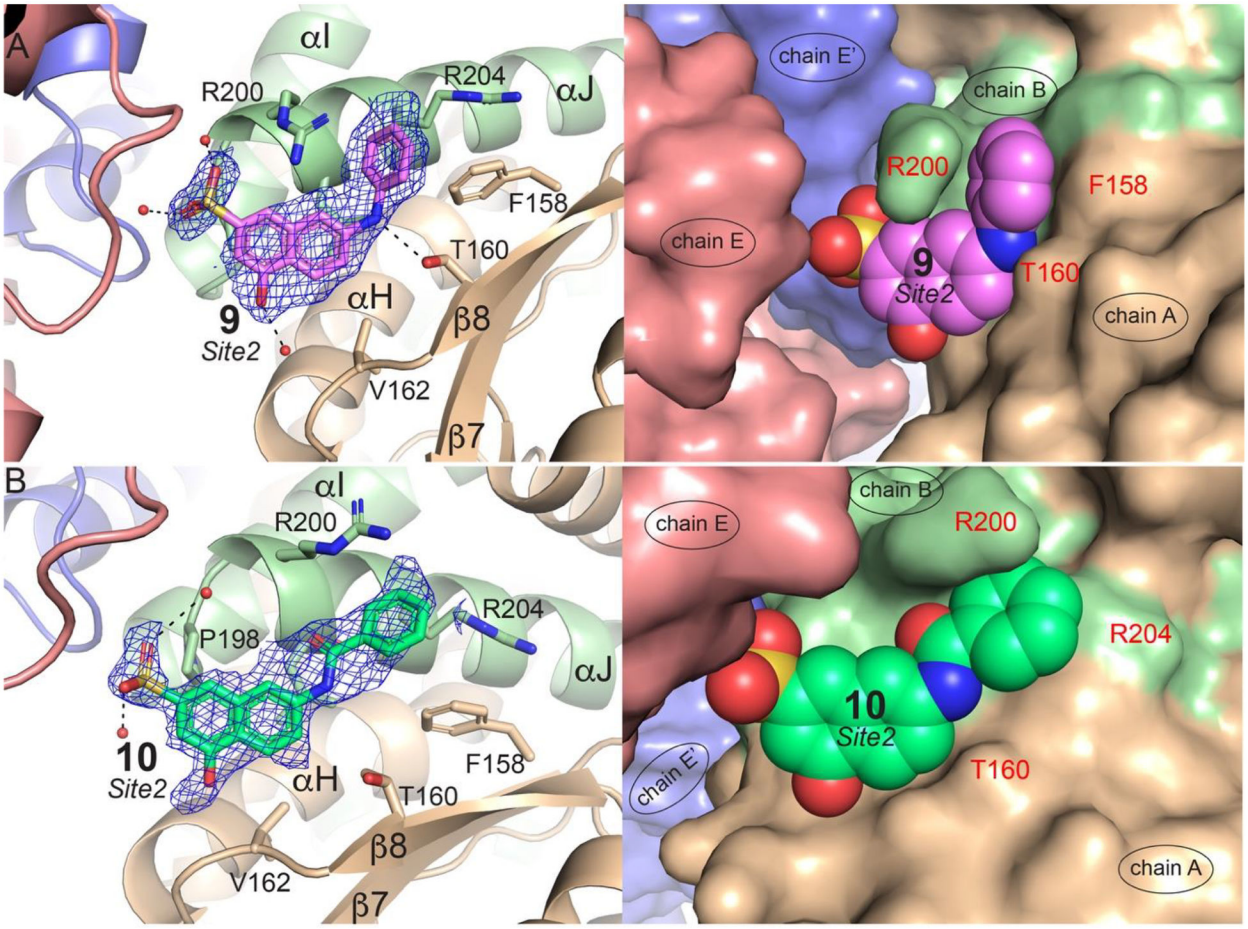

Figure 5.

The remote binding sites of compounds **9** and **10**. (A) Electron density (polder 3σ) and interactions for **9** in the binary PYCR1-**9** complex (pdb_00009p0s). (B) Electron density (polder 4σ) and interactions for **10** in the binary PYCR1-**10** complex (pdb_00009p0u). In all panels, the chains of the decamer have different colors.

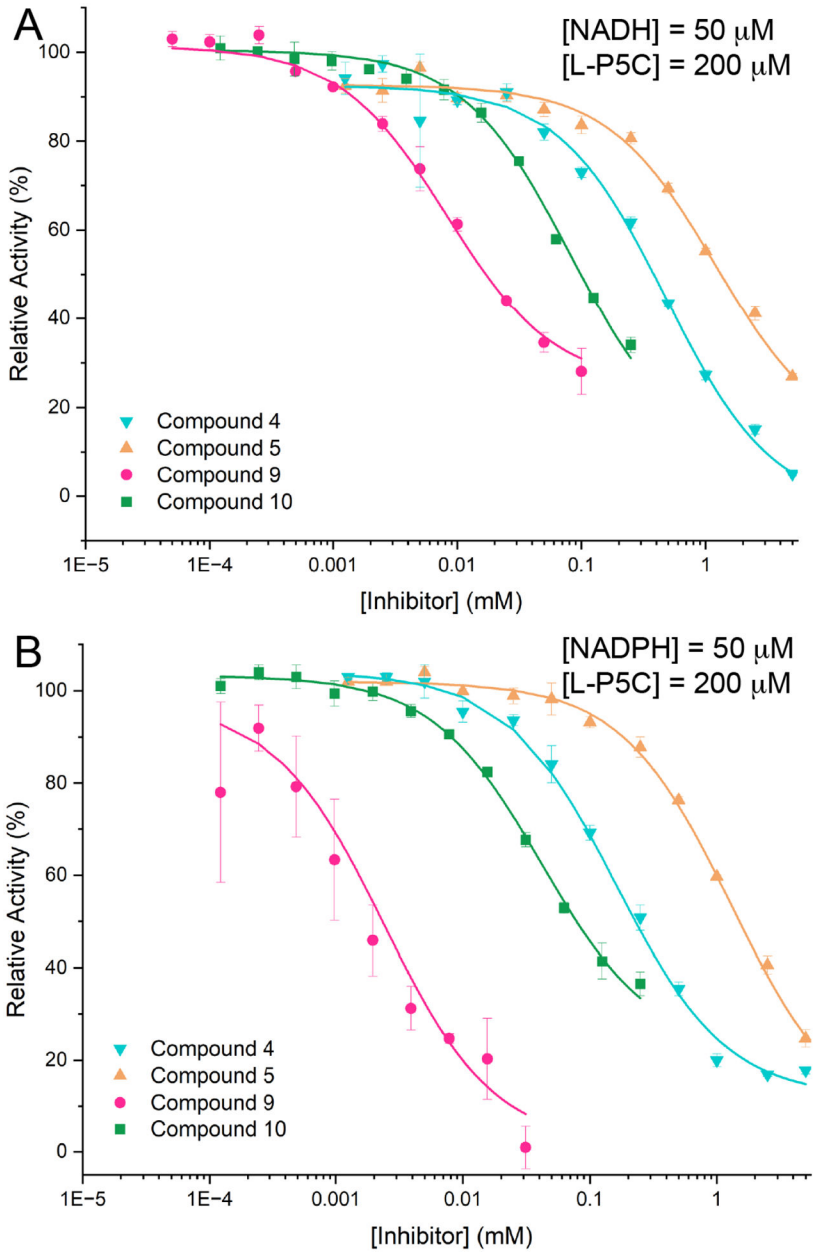

Figure 6.

Concentration-response plots for allosteric inhibitors using (A) NADH or (B) NADPH as the coenzyme. The error bars represent the standard deviation from three technical replicates. The data are normalized to the rate of PYCR1 in the absence of an inhibitor. IC_{50} values are listed in Table 3.

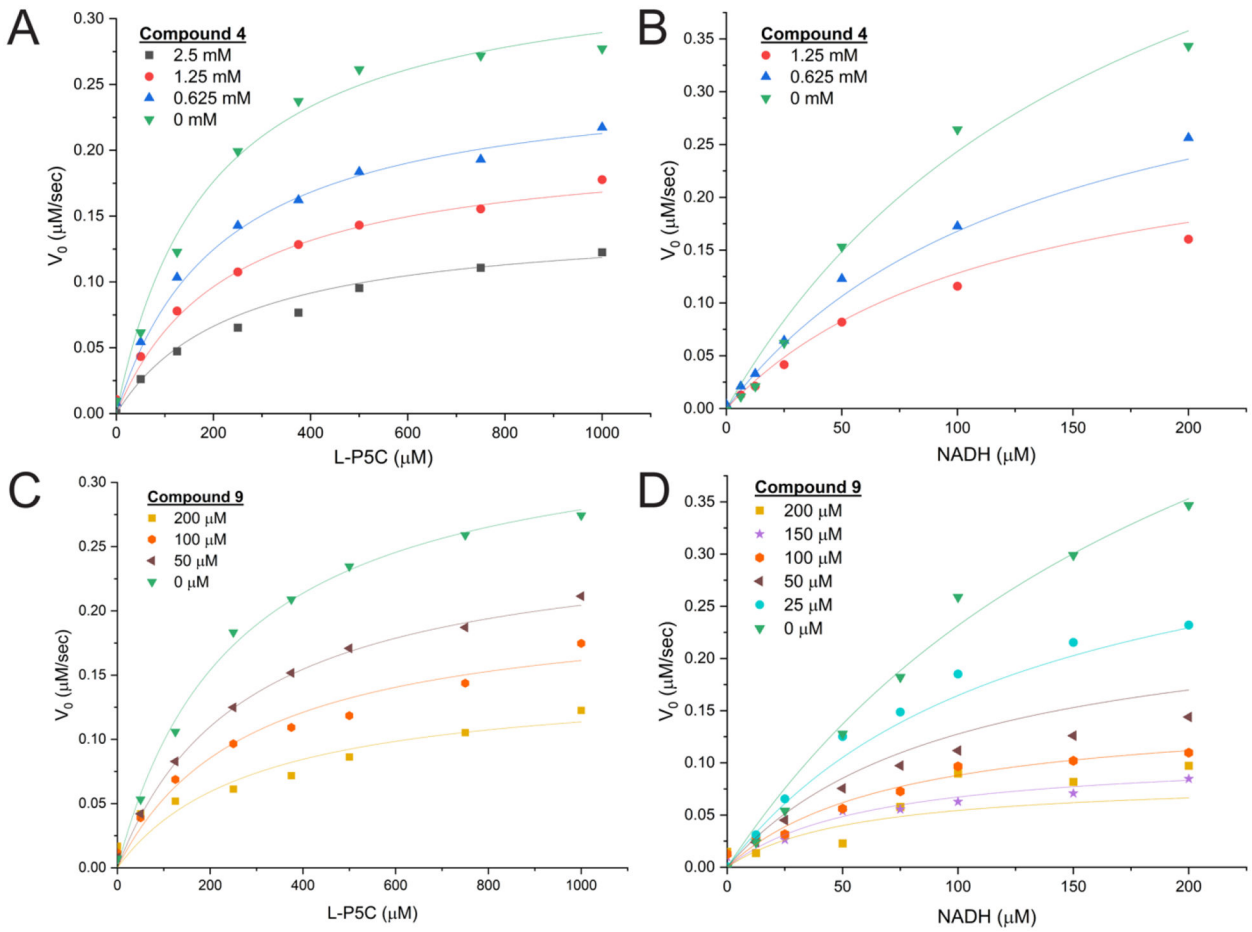

Figure 7.

Steady-state inhibition kinetics of PYCR1 by **4** (A,B) and **9** (C,D). L-P5C was the variable substrate in A and C, with NADH fixed at 175 μM. NADH was the variable substrate in B and D, with L-P5C fixed at 400 μM. The curves represent the global fits to the mixed model of inhibition (Equation 1). Inhibition parameters are listed in Table 4.

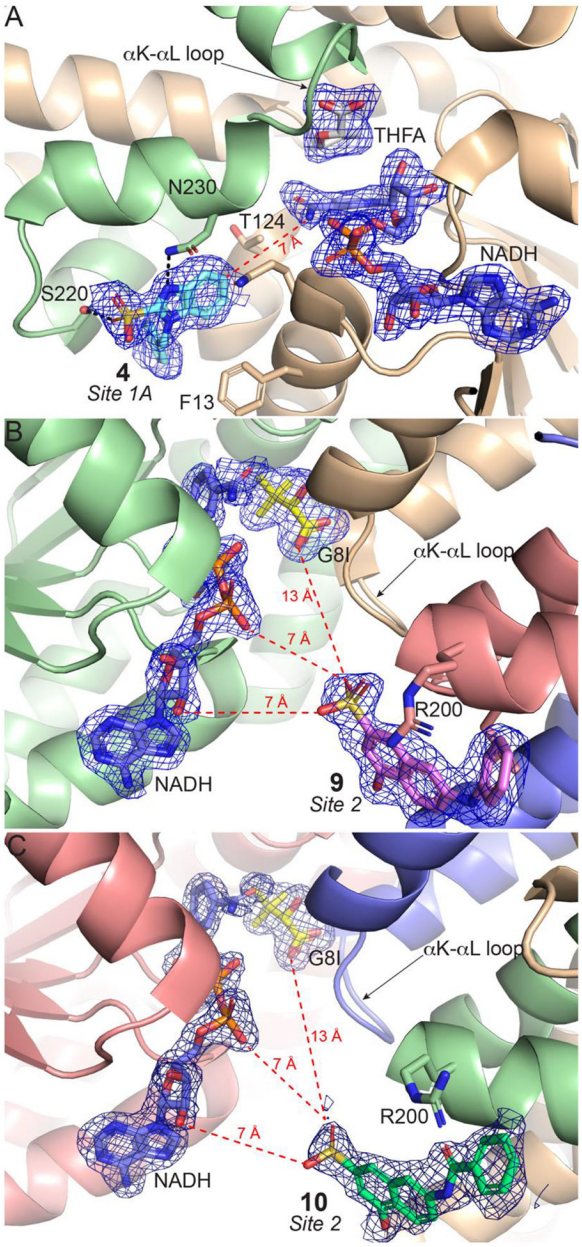

Figure 8.

Poses of allosteric inhibitors in the quaternary complexes. (A) PYCR1-**4**-NADH-THFA complex (pdb_00009q45). (B) PYCR1-**9**-NADH-G8I complex (pdb_00009p0t). (C) PYCR1-**10**-NADH-G8I complex (pdb_00009p0v). In all panels, the mesh represents a polder omit map (4σ) and the chains of the decamer have different colors. The red dashes indicate the closest distances between the inhibitor and the active site ligands (NADH, and the proline analogs THFA and G8I).

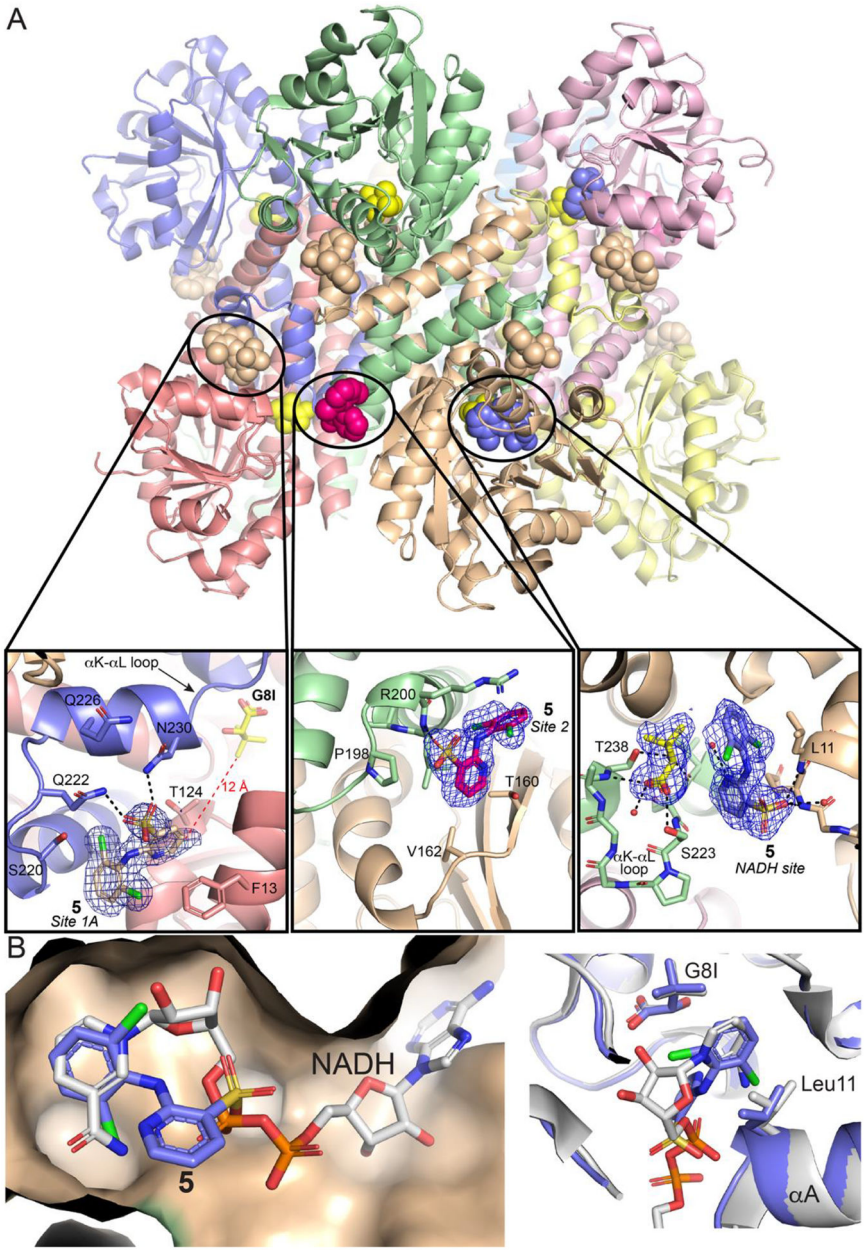

Figure 9.

Structure of the ternary PYCR1-**5**-G8I complex (pdb_00009q46). (A) The decamer viewed down a 2-fold axis. The poses of **5** are color coded according to the binding site as follows: wheat, Site 1A; hot pink, Site 2; blue, NADH site. The proline analog G8I is colored yellow. The insets show electron density (polder 4σ) for **5**. The red dashed line in the left inset indicates the closest distance between **5** and the proline analog G8I. The chains of the decamer have different colors. (B) Superposition of the ternary PYCR1-**5**-G8I complex (pdb_00009q46, blue) and the quaternary PYCR1-**9**-NADH-G8I complex (pdb_00009p0t, white) highlighting the overlap of **5** with NADH.

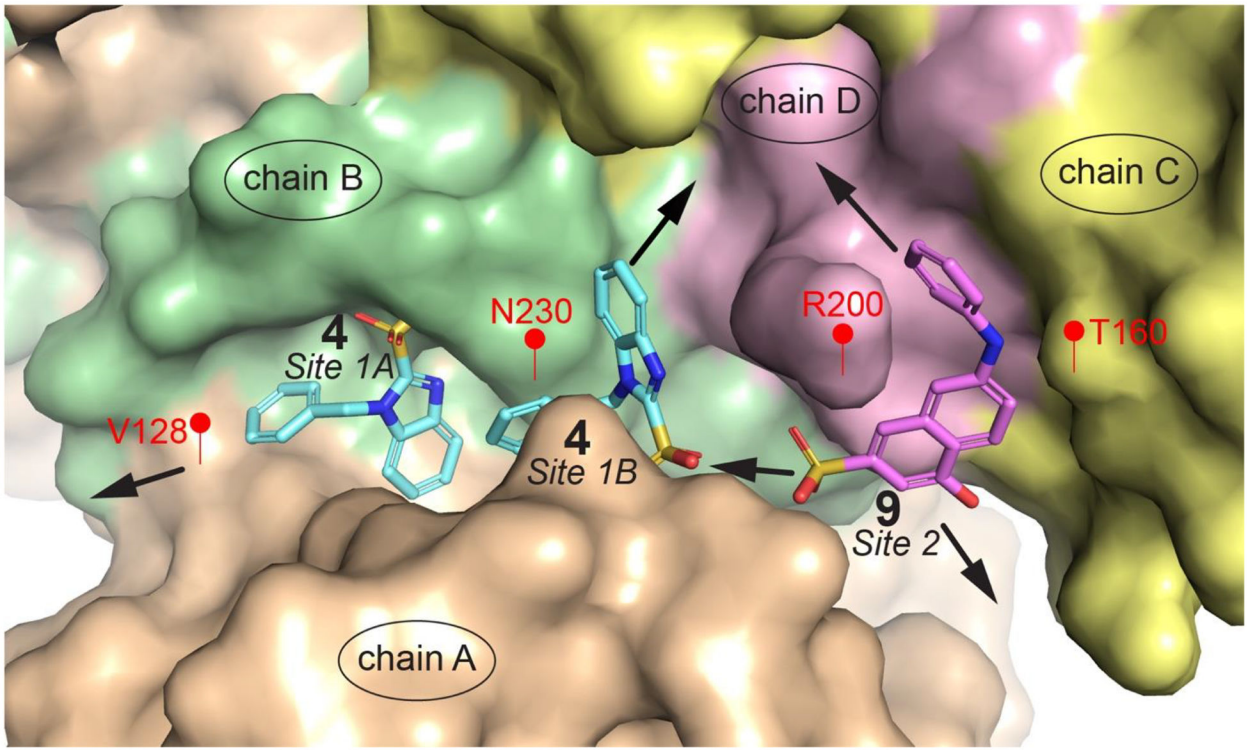

Figure 10.

Summary of the allosteric groove and potential growth vectors for elaborating the allosteric inhibitors. This figure was made from a composite model of the binary complexes of PYCR1 with **4** (pdb_00009p0q) and **9** (pdb_00009p0s). The chains of the decamer have different colors. Landmark residues of the allosteric groove are noted in red (Val128, Asn230, Arg200, and Thr160). The length of the groove as measured from Val128 to Thr160 is ~33 Å.

Table 1

X-ray diffraction data processing and refinement statistics for binary PYCR1-inhibitor structures

	4	5	9	10
Allosteric sites occupied	1A, 1B	1	2	2
Beamline	APS 24-ID-E	ALS 8.2.1	APS 24-ID-E	APS 24-ID-E
Space group	*C*2	*C*2	*C*2	*C*2
Unit cell parameters (Å,°)	*a* = 111.00 *b* = 181.01 *c* = 88.11 *β* = 106.65	a = 110.93 *b* = 180.80 *c* = 87.94 *β* = 106.53	*a* = 109.82 *b* = 179.48 *c* = 87.90 *β* = 106.45	*a* = 109.60 *b* = 179.59 *c* = 88.20 *β* = 106.49
Resolution (Å)	91.69–1.74 (1.77–1.74)	47.62–1.49 (1.52–1.49)	90.85–1.58 (1.61–1.58)	90.70–1.66 (1.69–1.66)
$R_{pim}(I)^a$	0.060 (0.534)	0.036 (0.871)	0.037 (0.521)	0.038 (0.530)
Mean I/σ^a	9.9 (1.5)	15.9 (0.9)	11.7 (1.5)	12.0 (1.5)
$CC_{1/2}{}^a$	0.996 (0.304)	0.999 (0.378)	0.998 (0.531)	0.999 (0.550)
Completeness (%)[a]	99.1 (99.9)	95.8 (80.8)	98.9 (98.3)	99.1 (99.0)
Multiplicity[a]	6.6 (6.6)	7.0 (6.3)	6.9 (7.0)	6.9 (6.8)
No. of protein residues	1380	1382	1381	1380
No. of non-H atoms				
Protein	9814	9838	9806	9786
Allosteric inhibitor	140	95	110	24
Water	795	961	726	735
$R_{cryst}/R_{free}{}^b$	0.200/0.224	0.195/0.221	0.181/0.196	0.183/0.203
RMSD bonds (Å)	0.007	0.006	0.006	0.006
RMSD angle (°)	0.856	0.809	0.833	0.822
Ramachandran plot[c]				
Favored (%)	97.88	98.76	98.25	98.39
Outliers (%)	0.07	0.00	0.00	0.07
Clashscore[c,d]	2.69 (99)	2.28 (99)	2.29 (99)	1.90 (99)
MolProbity Score[c,d]	1.27 (98)	1.10 (99)	1.21 (98)	1.12 (99)
Average *B* (Å^2)				
Protein	30.6	31.0	35.7	35.1
Allosteric inhibitor	31.0	33.8	37.6	33.6
Water	32.0	35.3	37.2	36.9
Inhibitor Occupancy	0.69–0.95	0.63–0.75	0.59–0.66	0.49
PDB ID	pdb_00009p0q	pdb_00009p0r	pdb_00009p0s	pdb_00009p0u

[a] Values for the outer resolution shell of data are listed in parentheses.

[b] 5% test set.

[c] From MolProbity.

[d] The percentile ranks are listed in parentheses.

Table 2

X-ray diffraction data processing and refinement statistics for quaternary and ternary complexes

	9 + NADH + G8I	**10 + NADH + G8I**	**4 + NADH + THFA**	**5 + G8I**
Allosteric sites occupied	2	2	1A	1A, 2
Beamline	APS 24-ID-E	APS 24-ID-E	APS 24-ID-E	APS 24-ID-E
Space group	*C*2	*C*2	*C*2	*C*2
Unit cell parameters (Å,°)	*a* = 112.54 *b* = 180.59 *c* = 88.11 *β* = 106.62	*a* = 111.76 *b* = 180.37 *c* = 88.21 *β* = 106.46	*a* = 111.04 *b* = 179.74 *c* = 88.22 *β* = 106.77	*a* = 110.77 *b* = 180.31 *c* = 88.14 *β* = 106.52
Resolution (Å)	92.59–1.79 (1.82–1.79)	92.14–1.80 (1.83–1.80)	91.51–1.79 (1.82–1.79)	90.15–1.75 (1.78–1.75)
$R_{pim}(I)^a$	0.073 (0.551)	0.040 (0.882)	0.072 (0.624)	0.067 (0.637)
Mean I/σ^a	9.2 (1.6)	13.8 (1.1)	8.6 (1.4)	7.9 (1.1)
$CC_{1/2}{}^a$	0.995 (0.229)	0.999 (0.515)	0.997 (0.257)	0.995 (0.302)
Completeness (%)[a]	98.7 (98.1)	99.3 (97.7)	99.4 (99.5)	99.2 (99.8)
Multiplicity[a]	6.8 (6.8)	6.9 (6.7)	6.9 (6.7)	6.9 (6.9)
No. of protein residues	1377	1387	1387	1384
No. of non-H atoms				
Protein	10009	9981	9931	9785
NADH	220	220	220	N/A
Proline analog	45	45	40	45
Allosteric inhibitor	110	168	40	171
Water	894	899	839	865
$R_{cryst}/R_{free}{}^b$	0.195/0.223	0.173/0.201	0.197/0.225	0.199/0.217
RMSD bonds (Å)	0.007	0.007	0.006	0.007
RMSD angle (°)	0.892	0.867	0.851	0.82
Ramachandran plot[c]				
Favored (%)	98.32	98.33	97.60	97.67
Outliers (%)	0.00	0.00	0.07	0.07
Clashscore[c,d]	2.71 (99)	1.36 (100)	2.12 (99)	2.72 (99)
MolProbity Score[c,d]	1.24 (99)	0.92 (100)	1.07 (100)	1.30 (98)
Average B (Å^2)				
Protein	25.9	29.8	30.2	32.8
NADH	26.2	31.6	30.5	N/A
Proline analog	22.7	27.3	30.0	25.8
Allosteric inhibitor	30.1	33.1	35.9	37.4
Water	30.4	34.8	34.0	35.2
Ligand occupancy				
NADH	0.89–1.00	0.76–0.92	1.00	N/A
Proline analog	1.00	1.00	1.00	0.61–1.0
Allosteric inhibitor	0.77–0.85	0.60–0.69	0.68–0.72	0.62–0.76

	9 + NADH + G8I	10 + NADH + G8I	4 + NADH + THFA	5 + G8I
PDB ID	pdb_00009p0t	pdb_00009p0v	pdb_00009q45	pdb_00009q46

[a] Values for the outer resolution shell of data are listed in parentheses.

[b] 2% or 5% test set.

[c] From MolProbity.

[d] The percentile ranks are listed in parentheses.

Table 3

Concentration-response results for compounds **4**, **5**, **9**, and **10**[a]

Compound	Coenzyme	IC_{50} (μM)[b]
4	NADH	478 ± 33
5	NADH	1208 ± 118
9	NADH	8.2 ± 1.3
10	NADH	81.5 ± 6.9
4	NADPH	161 ± 18
5	NADPH	1298 ± 106
9	NADPH	2.4 ± 0.8
10	NADPH	41.7 ± 3.8

[a]The concentration of the coenzyme NADH or NADPH was 50 mM. The concentration of L-P5C was 200 mM.

[b]The uncertainties are the standard parameter errors from nonlinear curve fitting in Origin. Three technical replicates were performed.

Table 4

Steady-state kinetic inhibition parameters for compounds **4** and **9** using the mixed model

Compound	Varied substrate[a]	Fixed substrate[a]	K_i (μM)[b]	α[b]	αK_i (μM)[b]
4	L-P5C	NADH	1200 ± 300	1.5 ± 0.5	1800 ± 750
9	L-P5C	NADH	110 ± 30	1.3 ± 0.5	143 ± 67
4	NADH	L-P5C	2000 ± 1000	0.4 ± 0.4	800 ± 900
9	NADH	L-P5C	160 ± 80	0.2 ± 0.1	32 ± 23

[a] When L-P5C was varied, NADH was fixed at 175 μM. When NADH was varied, L-P5C was fixed at 400 μM.

[b] The uncertainties are the standard parameter errors from nonlinear curve fitting in Origin. Technical replicates were not performed.